 CMES, vol.48, no.3, pp.303-336, 2009

Constitutive Contact Laws in Structural Dynamics

K. Willner[1]

Abstract: The dynamic behavior of structures with joints is strongly influenced by the constitutive behavior within the contact areas. In this paper the influence of an elaborate constitutive contact model based on a rough surface model is investigated. The contact model is able to describe several effects like pressure dependent contact stiffness in normal and tangential direction as well as microslip effects. The corresponding constitutive contact laws are implemented in a finite element code. Numerical simulations are compared to experimental results of a clamped double-beam experiment.

Keywords: Structural dynamics, damping, joints, friction.

1 Introduction

The main source of damping in typical engineering structures is structural damping which is based on energy dissipation in joints. A joint in this context is any contact area within the structure where relative displacements can take place, usually a bolted, riveted or otherwise clamped connection between different parts of the structure. Dissipation of energy is then mainly due to friction during relative displacements in tangential direction, i.e. slip. Even if large relative displacements are usually not desirable, small local slip will still contribute significantly to the overall energy dissipation. This behavior is called *microslip*, characterized by partial slip of the contact area while a large portion is still sticking thus ensuring structural integrity. Slipping of the complete contact area is called *macroslip* and is usually not allowed for obvious reasons except for cases where joints have specifically introduced and designed to act as friction dampers. While these basic mechanisms of structural damping are fairly well understood, a generally accepted modelling technique is not available and quantitative prediction of the damping by numerical simulations is still not possible or at least difficult.

The present state-of-the-art in joint modelling is documented in some recent review articles [Feeny, Guran, Hinrichs, and Popp (1998); Gaul and Nitsche (2000, 2001);

[1] Universität Erlangen-Nürnberg, Germany

Ibrahim and Pettit (2005); Mackerle (2003)]. But even if attempts to model the damping behavior of joints date well back in time and a huge number of publications in this area is available, the problem is still not completely solved and presents an open and active field of research, as several white papers show [Dohner (2001); Segalman, Paez, Smallwood, Sumali, and Urbina (2003)].

For joints with dimensions small compared to the jointed structure several phenomenological models are available to describe the global constitutive behavior of a complete joint. The simple Jenkin model [Jenkin (1922)] can be combined in parallel or series form [Iwan (1966, 1967); Berger and Krousgrill (2002); Miller and Quinn (2009); Quinn and Segalman (2005); Segalman (2005, 2006); Song, McFarland, Bergman, and Vakakis (2005)], or regularized to obtain better numerical and fitting properties [Gaul and Lenz (1997); Mayer and Gaul (2007)]. Other approaches include the Bouc-Wen model [Bouc (1957); Wen (1989)] discussed in detail by Ikhouane and Rodellar (2007) or the Dahl model [Dahl (1976); Bliman (1992)] and the LuGre model [de Wit, Olsson, Aström, and Lischinsky (1995)]. The parameters of these models have to be identified from experiments [Jalali, Ahmadian, and Mottershead (2007); Lobitz, Gregory, and Smallwood (2001); Ma, Bergman, and Vakakis (2001)], but the identification is usually difficult due to significant scatter and the use of uncertain parameters has been advised [Hanss, Oexl, and Gaul (2002)].

Models for extended joints usually require a dicretization of the contact surface using finite elements, since analytical solutions are hard to obtain. A notable exemption is the Menq model [Menq, Bielak, and Griffin (1986)], which gives an analytical solution for an extended lap joint. However, even for the very simple geometry used in this model the solution becomes quite involved, indicating that for real geometries and loading cases an analytical solution becomes impossible.

Since only small displacements are involved and generation of conforming meshes is usually not a problem, it is not necessary to turn to the arsenal of general contact formulations within the finite element framework, but the use of thin-layer [Ahmadian, Ebrahimi, Mottershead, and Friswell (2002); Ahmadian, Mottershead, James, Friswell, and Reece (2006)] or zero-thickness elements [Mayer and Gaul (2007)] is more efficient. Again the constitutive behavior within the contact area has to be modelled by suitable contact laws, but now on a local scale. In principle all of the global models mentioned above can be used on the local element scale as well, but usually only a simple elastic stick-slip law resembling a local Jenkin-element in conjunction with a linear normal stiffness is employed. Exemptions are the works by Sellgren and Olofsson (1999) who use a microslip model based on a stochastic surface model; and Lenz and Gaul (1995), and Mayer and Gaul (2007) using a regularized Masing model fitted to experimental data. An alternative approach is

presented by Garikipati (2002) who directly includes the micromechanical behavior into the continuum formulation using a variational multiscale approach. While this is a very elegant formulation, it is hard to include within a conventional finite element framework where the more traditional approach using constitutive laws allows for an easy and modular implementation.

In the following, constitutive contact laws in normal and tangential direction shall be employed which are identified from an elasto-plastic deformation model of the rough contact surfaces. The elasto-plastic contact is based on a halfspace model [Willner (2004, 2008b,a)] which has been also experimentally verified [Görke and Willner (2008b,a)]. The idea is to obtain suitable contact laws from a-priori information, like roughness and material data of the contacting surfaces. Employing these contact laws in a finite element simulation of the dynamic behavior of a joint should then give an accurate picture of the structural damping. As an example of an extended joint a simple double-beam experiment is chosen, which will be described next.

2 Experimental set-up

To exemplify the statements made in the introduction with regard to the damping of joints, a simple double-beam experiment is conducted. The double-beam consists of two equal beams made of stainless steel jointed by three bolts and clamped on one end as shown in Fig. 1. This type of experiment is quite popular [Pian and Hallowell (1951); Earles and Beards (1970); Ferri and Bindemann (1992); Song, Hartwigsen, McFarland, Vakakis, and Bergman (2004)], since it is the most simple model of a joint with an extended contact surface. The reason for choosing two equal beams is twofold. While for a fully clamped situation the interface between two equal beams would be the neutral axis, it also carries the maximum shear stress. So, due to the relatively low contact pressures used in the experiment the friction limit will be reached over a reasonable part of the contact area and there will be a considerable amount of slip. The other reason is just ease of identification of the parameters of the single beams which has to be done just once in a symmetric case. This is especially true for the Rayleigh damping parameters which are used to characterize other damping effects. These are considered to be structural and not material parameters and had to be determined twice if two different beams are used.

Principal dimensions of the set-up are given in Fig. 2. The bolt forces are adjusted using torque-control ($M_B = 2\,\mathrm{Nm}$) to $F_B \approx 1600\,\mathrm{N}$ each. The beam is excited by the impact of a modal hammer at the free tip (Point A in Fig. 2) and is then allowed to perform free vibrations, while a laser vibrometer measures the decay behavior of the tip displacement. While in principle also static load-displacement experi-

ments could be used to obtain information on the interface behavior, the available experimental equipment did not allow a sufficiently accurate measurement of the static deflections for a given load, therefore no attempt has been made to use this information.

Fig. 3 shows a plot of the tip displacement vs. time for the double-beam set-up in comparison to an equivalent monolithic beam in the same set-up. Clearly, the double-beam shows much higher damping due to frictional energy dissipation in the interface between the two beams. The aim of the following investigations is to predict this frictional damping behavior using *a-priori* information.

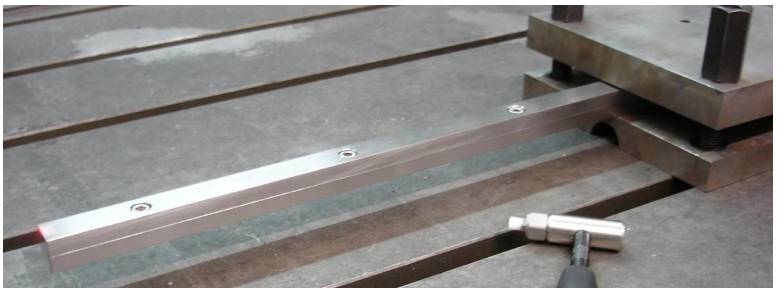

Figure 1: Double-beam experiment

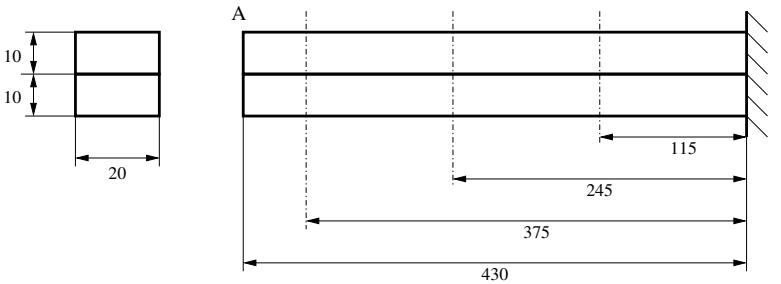

Figure 2: Double-beam dimensions

3 Contact model

The frictional damping in joints depends strongly on the roughness and material properties of the contacting surfaces. Thus, in a first step some aspects of a suitable surface description are discussed. Then a quite general simulation approach for the elasto-plastic contact behavior of rough surfaces is presented, which is based on

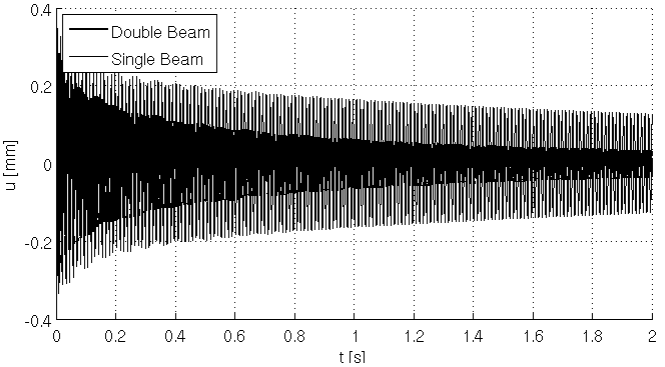

Figure 3: Comparison of decay behavior

a halfspace model. Typical results for roughness and material data corresponding to the surfaces of the double-beam experiment are presented. Finally, appropriate constitutive contact formulations are discussed, which can be used in a finite element simulation.

3.1 Fractal surface description

Most engineering surfaces show a characteristic scaling behavior over a wide range of length scales, which is known as self-affine or fractal. The concept of fractals was introduced by Mandelbrot (1983) and subsequently used to describe technical surfaces, see Ling (1987). Actually, the first contact model using a deterministic fractal description of rough surfaces was the one by Archard (1957), but it was presented well before the invention of the term fractal. Recent contributions prefer stochastic fractals mostly based on spectral representations, like the works by Ju and Farris (1996); Stanley and Kato (1997); Jackson and Kogut (2006), but other forms are also know like the Cantor-set model of Warren and Krajcinovic (1996). The popular Weierstrass function model is a special case of a spectral representation, see Majumdar and Tien (1990); Komvopoulos and Ye (2001); Ciavarella, Demelio, Barber, and Jang (2000).

The scaling behavior of a roughness profile can be described by the so-called structure function given for a discrete profile $z_k = z(x_k)$ by

$$S(x_k) = \frac{1}{N-k} \sum_{i=1}^{N-k} (z_{i+k} - z_i)^2 \qquad k = 1, \ldots, N-1 \; . \tag{1}$$

As an example a spark-eroded aluminum surface was measured using a conven-

tional stylus profilometer and on a much smaller scale using an atomic force microscope (AFM), see Figs. 4 and 5, respectively.

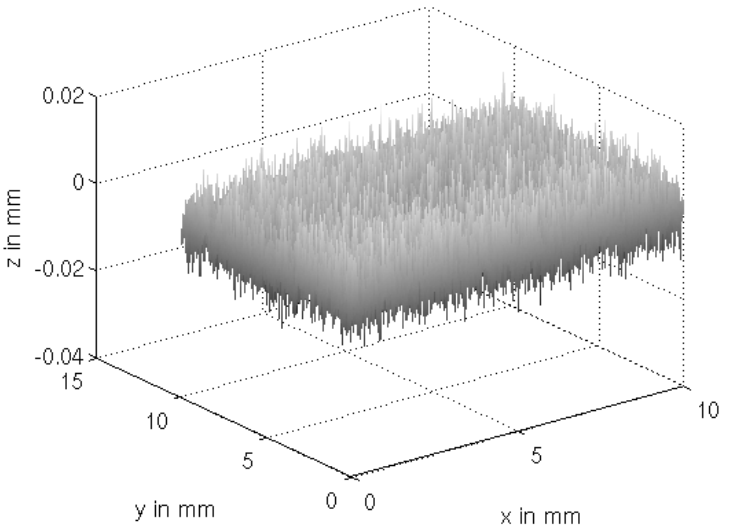

Figure 4: Stylus profilometer measurement of spark eroded aluminum surface

Calculating the structure function along various profiles shows a typical mixed fractal-regular behavior, see Fig. 6. For small values of x, i.e. small correlation lengths, the structure function is a straight line in a log-log plot, which is characteristic for a fractal, with the slope corresponding to the fractal dimension. For large values of x, i.e. large correlation lengths, however, the surface shows a regular or stationary behavior, indicated by a constant value of the structure function. A closer inspection shows that this value is actually $2\sigma_z^2$, where σ_z is the standard deviation of the height distribution. Thus, a typical engineering surface shows fractal behavior for small length scales, but becomes stationary at larger length scales, see Wang and Komvopoulos (1994); Willner (2008b).

Measured structure functions of this type can be approximated quite well by an analytical function proposed by Berry and Blackwell (1981),

$$S(x) = 2\sigma_z \left\{ 1 - \exp\left[-\left(\frac{x}{x_T} \right)^{4-2D} \right] \right\} \tag{2}$$

where D is the fractal dimension and x_T is the transition length scale between fractal and regular behavior, see Fig. 7.

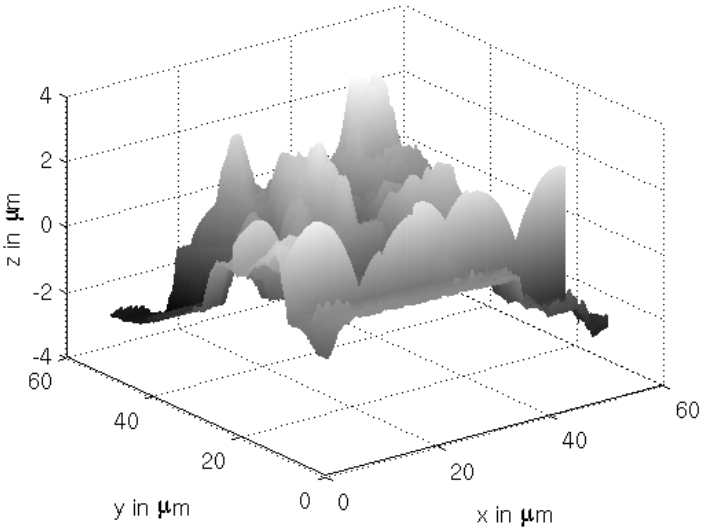

Figure 5: AFM measurement of spark eroded aluminum surface

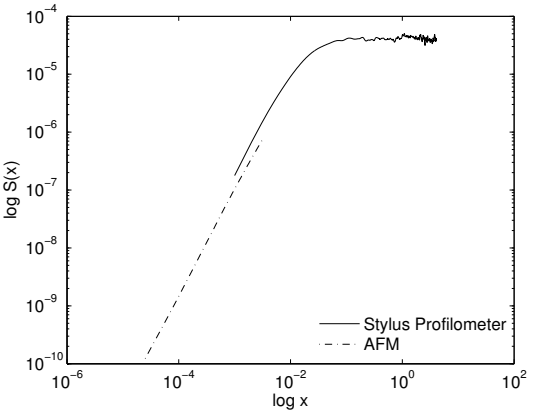

Figure 6: Structure function of spark eroded aluminum surface

The three parameters σ_z, D and x_T are sufficient to characterize at least an isotropic Gaussian surface and can be used to generate virtual surfaces with specified characteristics for parameter studies, see Willner (2004, 2008b). Extensions to anisotropic and non-Gaussian surfaces are possible.

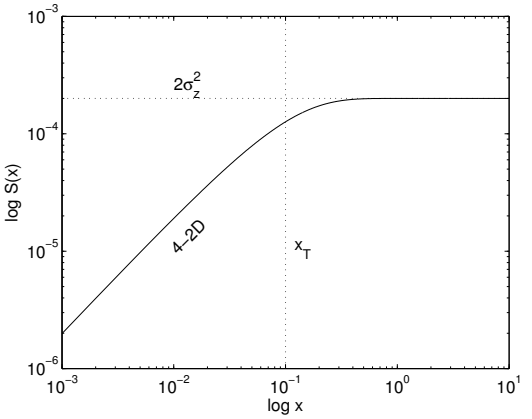

Figure 7: Berry-Blackwell approximation of structure function

3.2 Halfspace model

The constitutive contact behavior of rough surfaces, either measured or numerically generated, can be simulated efficiently using halfspace modeling based on the Boussinesq and Cerruti solutions. Different techniques are known, see for example Webster and Sayles (1986); Ogilvy (1992); Ren and Lee (1993); Lee and Ren (1996); Varadi and Neder (1996), Polonsky and Keer (2000a), Jacq, Nelias, Lormand, and Girodin (2002), Karpenko and Akay (2002), Li and Berger (2003); Wang and Keer (2005); Nelias, Antaluca, Boucly, and Cretu (2007); and the survey articles of Sayles (1996); Polonsky and Keer (2000b); and Allwood (2005). Here a model based on the work of Kalker and van Randen (1972) will be used. This model was again discussed by Kalker (1977) for the frictionless normal contact and later extended to frictional contact by Kalker (1979), Vollebregt (1995) and Willner (2008a). Plasticity was introduced by Tian and Bhushan (1996), Willner (2004) and Sainsot, Jacq, and Nelias (2002).

3.2.1 Normal contact

We consider first the frictionless normal contact of a rough elastic surface with a smooth rigid wall, as shown in Fig. 8. The roughness is given by height coordinates $z(x,y)$, where the height coordinates are taken relative to the mean plane of the surface, such that

$$\text{mean}(z) = 0\,. \tag{3}$$

Further we define as gap distance g the separation of the mean plane of the rough

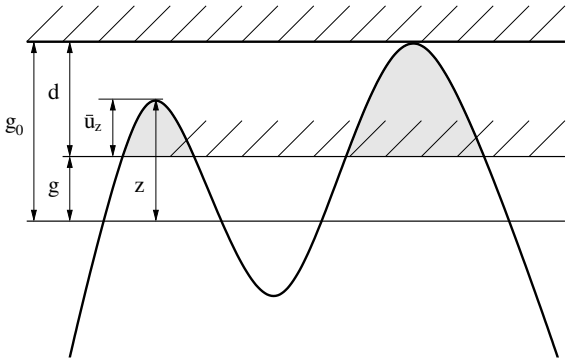

Figure 8: Normal contact

surface and the rigid wall, where g_0 is the initial separation when the surface just touches the wall, which is equal to

$$g_0 = \max(z) \; . \tag{4}$$

The approach d of the surface is then defined by

$$d = g_0 - g \tag{5}$$

and the local geometrical interference at a given approach is

$$\bar{u}_z(x,y) = z(x,y) - (g_0 - d) \; , \tag{6}$$

Since a positive interference means an overlap of the undeformed surface with the wall, it indicates the potential contact area, while a negative interference means separation.

Now, we have to find a contact pressure distribution such that the local geometrical interference of the deformed surface is zero or negative everywhere, where a zero interference indicates contact, while a negative interference indicates separation. The halfspace contact model used here is based on a variational approach using the minimization of the total complementary potential energy V^* given by

$$V^* = \int_{\Omega} U^*(\sigma_{ij}) \, \mathrm{d}\Omega - \int_{\Gamma} t_i \bar{u}_i \, \mathrm{d}\Gamma \; , \tag{7}$$

where $U^*(\sigma_{ij})$ is the internal complementary energy density within the elastic domain Ω, and t_i and $\bar{u}_i$ are surface tractions and prescribed displacements on the contact surface Γ, respectively.

Introducing a suitable surface discretization of the potential contact area into M equal patches as shown by Kalker (1990); Tian and Bhushan (1996); and Willner (2004) gives

$$V^* = \frac{1}{2}\mathbf{p}^{\mathrm{T}}\mathbf{C}^{(zz)}\mathbf{p} - \mathbf{p}^{\mathrm{T}}\bar{\mathbf{u}}_z \,, \tag{8}$$

where $\mathbf{C}^{(zz)}$ is the normal flexibility matrix and $\mathbf{p}$ contains the pressures on the contact patches of the surface discretization. Minimization of this functional leads finally to

$$\mathbf{C}^{(zz)}\mathbf{p} = \bar{\mathbf{u}}_z \,, \tag{9}$$

which is solved by a Gauss-Seidel iteration for the unknown pressures $\mathbf{p}$. During the iteration the additional restrictions

$$p_l \geq 0 \,, \qquad l = 1,\ldots,M \tag{10}$$

have to be observed, since no tension is allowed at the interface. Convergence of the iteration procedure is assured [Kalker (1990)] and the contact elements with positive pressure finally form the real area of contact.

This purely elastic algorithm can be extended to incorporate plastic contact [Tian and Bhushan (1996); Willner (2008b)] by adjusting the height data iteratively to ensure that the local pressure remains below a certain maximum local pressure, usually termed as hardness H,

$$p_l \leq H \,, \qquad l = 1,\ldots,M \,. \tag{11}$$

While this adjustment is not volume conserving, it gives good results which are confirmed by experimental results, see Görke and Willner (2008a,b). The rationale is that the plastically displaced material is moved into the valleys of the roughness and therefore does not influence the contact. This assumption is valid as long as the fraction of real contact area is small, say $\alpha < 0.1$.

Since only the contact behavior of the rough contact surface is of interest, the bulk deformation has to be subtracted. This can be achieved by an iterative correction discussed by Ren and Lee (1994).

The contact between two rough surfaces can be simulated by just adding the roughness data

$$z(x,y) = z_1(x,y) + z_2(x,y) \,, \tag{12}$$

since only the gap distance is necessary, and using an equivalent Hertzian modulus given by

$$\frac{1}{E^*} = \frac{1}{E_1^*} + \frac{1}{E_1^*} \,. \tag{13}$$

3.2.2 Frictional contact

The procedure presented above for the pure normal contact can be extended to the fully coupled contact problem with friction.

Replacing the normal pressure p and normal displacement u_z by the full surface traction vector $\vec{t}$ including the in-plane tractions q_x and q_y

$$\vec{t} = q_x \vec{e}_x + q_y \vec{e}_y + p \vec{e}_z \tag{14}$$

and the corresponding full surface displacement vector

$$\vec{u} = u_x \vec{e}_x + u_y \vec{e}_y + u_z \vec{e}_z \,, \tag{15}$$

respectively, we obtain the expression for the complementary energy as

$$V^* = \frac{1}{2} \int_\Gamma \vec{t} \cdot \vec{u} \, \mathrm{d}\Gamma - \int_\Gamma \vec{t} \cdot \vec{\bar{u}} \, \mathrm{d}\Gamma \,, \tag{16}$$

where $\vec{\bar{u}}$ is now the prescribed relative displacement between the elastic surface and the rigid wall including tangential components.

Introducing the same surface discretization as before, the fully coupled displacement-traction relationship can be written as

$$u_{xk} = \sum_{l=1}^{M} \left(C_{kl}^{xx} q_{xl} + C_{kl}^{xy} q_{yl} + C_{kl}^{xz} p_l \right) \tag{17}$$

$$u_{yk} = \sum_{l=1}^{M} \left(C_{kl}^{yx} q_{xl} + C_{kl}^{yy} q_{yl} + C_{kl}^{yz} p_l \right) \tag{18}$$

$$u_{zk} = \sum_{l=1}^{M} \left(C_{kl}^{zx} q_{xl} + C_{kl}^{zy} t_{yl} + C_{kl}^{zz} p_l \right) \tag{19}$$

or in matrix form as

$$\begin{bmatrix} \mathbf{u}_x \\ \mathbf{u}_y \\ \mathbf{u}_z \end{bmatrix} = \begin{bmatrix} \mathbf{C}^{(xx)} & \mathbf{C}^{(xy)} & \mathbf{C}^{(xz)} \\ \mathbf{C}^{(yx)} & \mathbf{C}^{(yy)} & \mathbf{C}^{(yz)} \\ \mathbf{C}^{(zx)} & \mathbf{C}^{(zy)} & \mathbf{C}^{(zz)} \end{bmatrix} \begin{bmatrix} \mathbf{q}_x \\ \mathbf{q}_y \\ \mathbf{p} \end{bmatrix} \tag{20}$$

$$\mathbf{u} = \mathbf{C}\mathbf{t} \tag{21}$$

The elements of the flexibility matrix can be obtained from the complete Boussinesq solution for normal loading and the Cerruti solution for tangential loading, respectively [Dydo and Busby (1995); Li and Berger (2001); Willner (2008a)].

Using this approximation in the total complementary energy we obtain the discretized form as

$$V^* = \frac{1}{2}\mathbf{t}^{\mathrm{T}}\mathbf{C}\mathbf{t} - \mathbf{t}^{\mathrm{T}}\bar{\mathbf{u}} \,. \tag{22}$$

Minimization of this functional leads to

$$\mathbf{C}\mathbf{t} = \bar{\mathbf{u}} \,, \tag{23}$$

which is again solved by a Gauss-Seidel iteration for the unknown tractions $\mathbf{t}$. During the iteration the normal restriction

$$p_l \geq 0 \,, \qquad l = 1, \ldots, M \tag{24}$$

has to be observed, since again no tension is allowed at the interface. In tangential direction the restriction

$$\sqrt{q_{xl}^2 + q_{yl}^2} \leq q_{\max l} \tag{25}$$

has to be observed, where the local limit shear stress $q_{\max l}$ can be given for example by

- a local Coulomb condition

$$q_{\max l} = \mu p_l \tag{26}$$

- or a local Tresca condition

$$q_{\max l} = \tau_{\max} \,. \tag{27}$$

where μ is a local friction coefficient and $\tau_{\max}$ would be a pressure independent shear limit. Again, convergence of the iteration procedure is assured [Vollebregt (1995)].

As shown by Willner (2008a), it is usually not necessary to take into account the full coupling between normal and tangential loading. By employing the classical assumptions of Mindlin (1949), the tangential problem can be completely decoupled from the normal problem, such that the contact area is given by the normal load alone. Then, the tangential problem can be solved for a given pressure with a fixed contact area, thus simplifying the computations significantly.

3.3 Typical results

A representative section of the contact surface of one of the beams of the double-beam experiment was measured using an white-light interferometer, with the results shown in Fig. 9. The surface is clearly orthotropic due to the manufacturing process. However, in the double-beam set-up the joint surface will be nearly isotropic since the orthotropy directions are oriented under a right angle, see Fig. 10. By fitting the structure function (2) to the measured structure function, the roughness data for the joint surface can be identified as $\sigma_z = 1.22 \cdot 10^{-3}\,\mathrm{mm}$, $x_T = 0.02\,\mathrm{mm}$, and $D = 2.1$. However, for the following calculations the measured height data were used directly as input for the halfspace simulation.

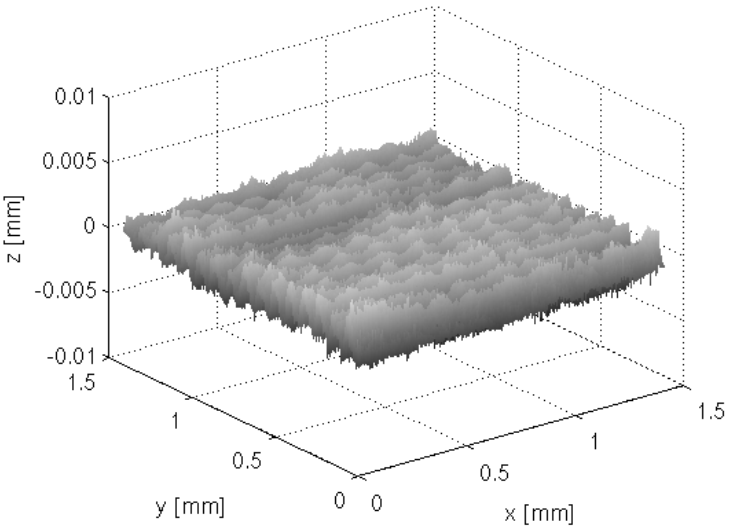

Figure 9: Measured surface of double-beam experiment

Figs. 11 and 12 show calculated elasto-plastic loading and unloading curves $\alpha(g)$ and $p(g)$, respectively, up to different nominal contact pressures p. Figs. 13 and 14 show the calculated tangential behavior for the loading and unloading case, respectively, for a maximum loading up to $p = 1\,\mathrm{N/mm^2}$.

These results were obtained by the decoupled Mindlin approach using material parameters given in Tab. 1 and a local Tresca condition for slip.

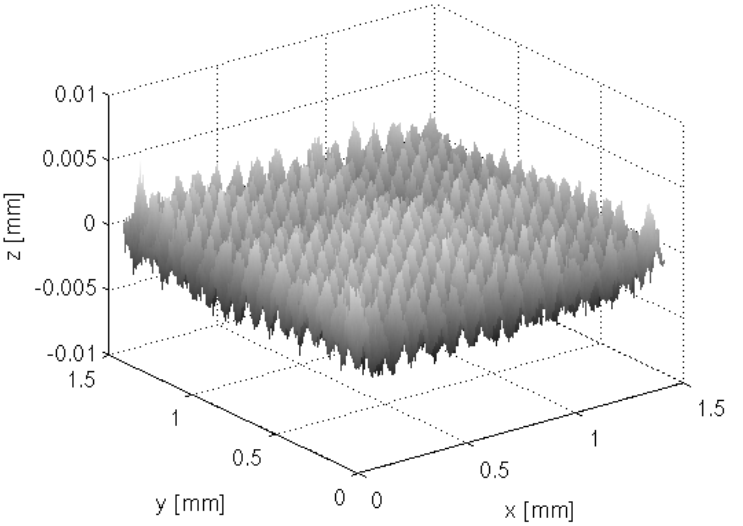

Figure 10: Joint surface of double-beam experiment

Table 1: Material parameters for contact simulation

E	ν	H	$\tau_{\max}$
$1.67 \cdot 10^5\,\mathrm{N/mm^2}$	0.3	$1000\,\mathrm{N/mm^2}$	$150\,\mathrm{N/mm^2}$

3.4 Constitutive contact laws

The results of the halfspace simulation of a specific contact pairing could be used directly in a finite element simulation of a structural joint, using for example tabulated values and interpolation. However, it is desirable to derive closed form approximations of a more general type. Specifically, we look for an expression describing the normal contact by a pressure-gap relation $p(g)$ which relates the nominal pressure p to the gap distance g, such that the negative derivative of this relation with respect to the gap distance is the normal contact stiffness,

$$C_n = -\frac{\mathrm{d}p}{\mathrm{d}g}\,. \tag{28}$$

Of similar interest is an expression which gives the fraction of real area of contact as a function of the gap distance $\alpha(g)$ or alternatively as a function of nominal pressure $\alpha(p)$. Likewise, for the tangential contact we are looking for an expression relating the nominal shear traction $t(u,g)$ to the relative tangential displacement u

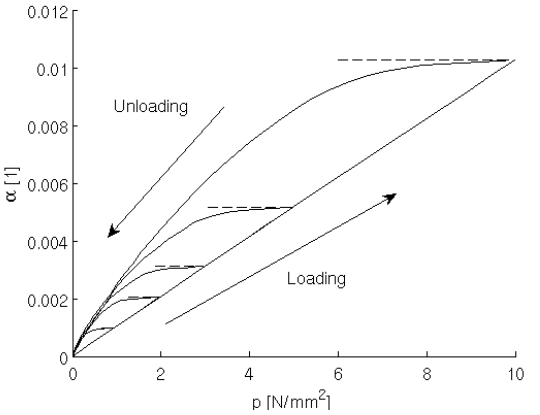

Figure 11: Elasto-plastic pressure-area relation (solid) and constant approximation (dashed) upon unloading (Eq. 37)

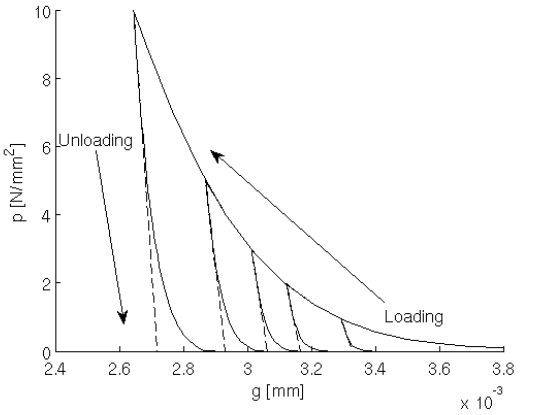

Figure 12: Elasto-plastic gap-pressure relation (solid) and linear approximation (dashed) upon unloading (Eq. 39)

and a given gap distance g, such that the derivative of this relation with respect to the relative displacement is the tangential stiffness,

$$C_t = \frac{\partial t}{\partial u} \,. \tag{29}$$

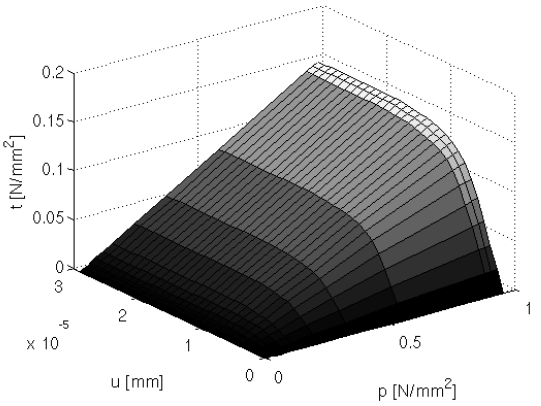

Figure 13: Traction-slip-pressure relation $t(u,p)$ for the initial loading case up to $p = 1\,\mathrm{N/mm^2}$

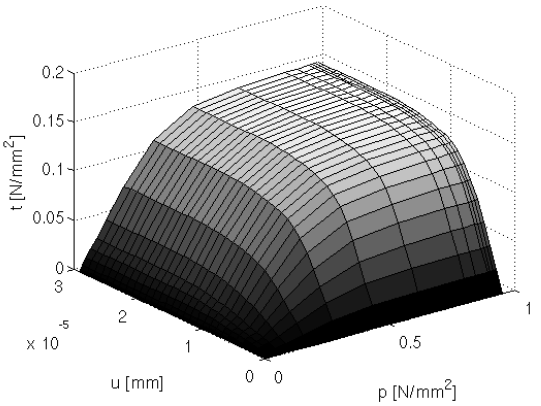

Figure 14: Traction-slip-pressure relation $t(u,p)$ for the unloading case from $p = 1\,\mathrm{N/mm^2}$

3.4.1 Normal contact

Willner (2008b) showed that for the purely elastic case the pressure-gap relations for isotropic fractal-regular surfaces can be approximated quite well by an exponential contact law of the BGT-type [Bush, Gibson, and Thomas (1975)]

$$p(\gamma) = \frac{E^*}{2\pi}\sqrt{\frac{m_2}{2}}\frac{1}{\gamma}\exp\left(-\frac{\gamma^2}{2}\right), \tag{30}$$

where γ is the normalized gap distance given by

$$\gamma = \frac{g}{\sigma_z} . \tag{31}$$

The parameter m_2 can be explicitly determined from the given structure function Eq. 2 for the *non-fractal limit* $D = 2$,

$$m_2 = 2\left(\frac{\sigma_z}{x_T}\right)^2 . \tag{32}$$

As numerical experiments show, the resulting approximation

$$p(\gamma) = \frac{E^*}{2\pi}\frac{\sigma_z}{x_T}\frac{1}{\gamma}\exp\left(-\frac{\gamma^2}{2}\right) \tag{33}$$

is also reasonable for the fractal case $2 < D < 3$, i.e. the fractal dimension has only a minor influence on the pressure-gap law.

The area-pressure relation is given in the BGT-model by

$$\alpha(p) = \frac{p}{E^*}\sqrt{\frac{\pi}{m_2}} \tag{34}$$

which becomes in view of Eq. 32

$$\alpha(p) = \sqrt{\frac{2}{\pi}}\frac{p}{E^*}\frac{x_T}{\sigma_z} . \tag{35}$$

Numerical results are in excellent agreement with this relation for the case $D = 2$. However, the numerical area-pressure relations do not converge for the case $2 < D < 3$, i.e. a fractal surface. Here, the real area of contact becomes a fractal itself with a fractal dimension $D < 2$, such that the contact area dissolves into an increasing large number of vanishing contact spots, where the local contact pressure rises to extreme values. This numerically obtained result [Willner (2004)] is also analytically confirmed [Borri-Brunetto, Carpinteri, and Chiaia (1998)].

The high local pressures for the fractal case indicate that an elastic solution is in general impossible but a plastic solution has to be used. Then, the area-pressure law upon initial loading can be fitted very well by

$$\alpha(p) = \frac{p}{H} , \tag{36}$$

indicating that elastic effects can be neglected, at least at the low nominal contact pressures occurring in structural joints. However, as Fig. 11 shows, this relationship

is not valid for the unloading and reloading case, which will be elastic anyway. But, since the contact area drops only slightly at the beginning of the unloading, a constant approximation

$$\alpha(p) = \alpha(p_{\max}) = \frac{p_{\max}}{H} = \text{const.} \tag{37}$$

depending on the maximum local pressure seems justified, if the local contact pressure does not vary significantly during operation. This approximation is shown by the dashed lines in Fig. 11.

Since a typical fractal surface will deform purely plastically upon initial loading, the pressure-gap law $p(\gamma)$ is given up to moderate loads $p < H/10$ by the bearing area curve (Abbott curve),

$$p(\gamma) = H \int_{\gamma}^{\infty} \Phi(\gamma) \mathrm{d}\gamma \,, \tag{38}$$

where $\Phi(\gamma)$ is the distribution of heights. However, upon unloading and reloading the deformation will be purely elastically. As Fig. 15 shows, the unloading stiffness, which can be obtained by numerically differentiating the corresponding unloading branch of the gap-pressure relation $p(g)$, will be nearly constant in the upper pressure range. Thus, a linear pressure-gap behavior,

$$p(g) = p_{max} - C(p_{max})(g - g_{min}) \,, \tag{39}$$

seems to be a reasonable approximation for the unloading case, which is shown by the dashed lines in Fig. 12. This relation depends on the plastic predeformation given by the pair $(g_{\min}, p_{\max})$, which play the role of state variables describing the irreversible evolution of the contact. As Fig. 16 shows, the normal stiffness $C_n(p_{max})$ can be fitted quite well by a function

$$C_n(p_{\max}) = \beta_1 \left(\frac{p_{\max}}{H} \right)^{\beta_2} \,, \tag{40}$$

where for the specific surface data used here $\beta_1 \approx 3.8 \cdot 10^6$ N/mm^3 and $\beta_2 \approx 0.7$.

3.4.2 Tangential contact

Fig. 13 shows that upon initial loading the maximum tangential traction $t_{\max}$ increases linearly with the pressure p in agreement with Coulomb's law. The reason is the underlying adhesion assumption of the halfspace model, where the maximum tangential traction at full slip is simply given by

$$t_{\max}(p) = \alpha(p)\tau_{\max} \,. \tag{41}$$

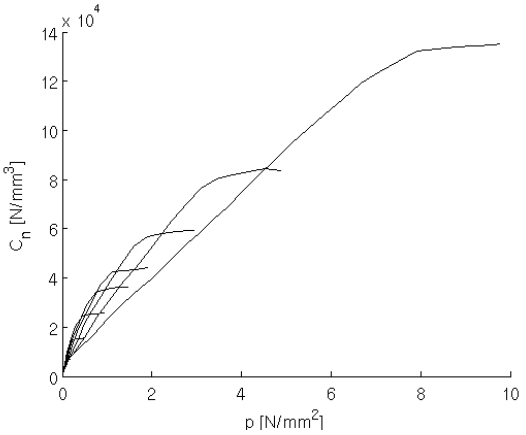

Figure 15: Normal stiffness at unloading as a function of normal pressure

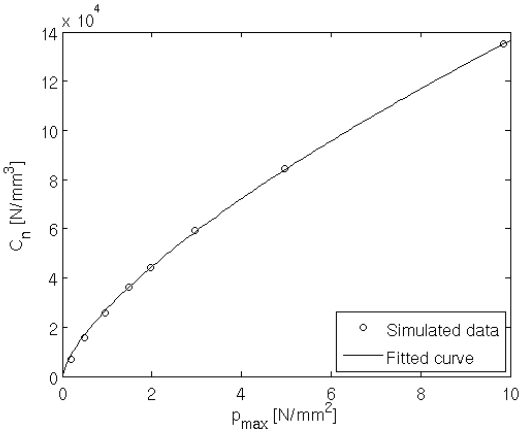

Figure 16: Maximum normal stiffness at unloading as a function of maximum preload

Using the area-pressure law Eq. 36 this can be rewritten as

$$t_{\max}(p) = \mu p \,, \tag{42}$$

with the friction coefficient given by

$$\mu = \frac{\tau_{\max}}{H} \,. \tag{43}$$

However, upon unloading the maximum tangential traction is constant over the upper pressure range, see Fig. 14, due to the fact that the contact area is here nearly

constant and given by Eq. 37. The maximum tangential traction depends then just on the maximum preload by

$$t_{\max}(p) = t_{\max}(p_{\max}) = \frac{p_{\max}}{H}\tau_{\max} = \text{const.} \tag{44}$$

Normalizing the tangential tractions by the maximum traction $t_{\max}$ and the relative tangential displacement u by a characteristic slip distance u_{sl}, the traction-slip relations for all pressures fall closely together as can be seen from Fig. 17. This tangential behavior can be adequately described by a regularized friction law with a linear behavior for elastic sticking, where the tangential stiffness for stick is pressure dependent and given by

$$C_t(p) = \frac{t_{\max}(p)}{u_{sl}} \,. \tag{45}$$

The characteristic slip distance u_{sl} can be identified from the halfspace simulations. For the unloading case it is only weakly dependent on the maximum preloading $p_{\max}$. Thus, it can be approximated quite well by a constant value $u_{sl} \approx 10^{-5}\,\text{mm}$ in the pressure range $p < 5\,\text{N/mm}^2$ of the double-beam experiment.

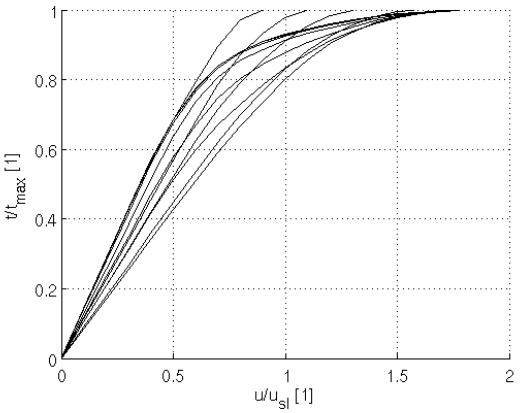

Figure 17: Normalized traction-slip relation for the unloading case from $p = 1\,\text{N/mm}^2$

4 Double-beam experiment

The constitutive contact laws derived above are now employed in a finite element simulation of the double-beam experiment presented in the introduction. The user-subroutine UINTER within the Finite-Element code ABAQUS has been used to

implement the nonlinear pressure-gap law given by Eq. 38 in the loading case and the linear pressure-gap law Eq. 39 with a pressure dependent normal stiffness given by Eq. 40, where the local maximum pressure $p_{\max}$ and minimum gap $g_{\min}$ are used as state variables. For the tangential contact a pressure dependent tangential stiffness given by Eq. 45 and a maximum local traction given by Eq. 44 has been implemented.

4.1 Finite element model

Figure 18 shows the finite element mesh and the initial displacement of the set-up.

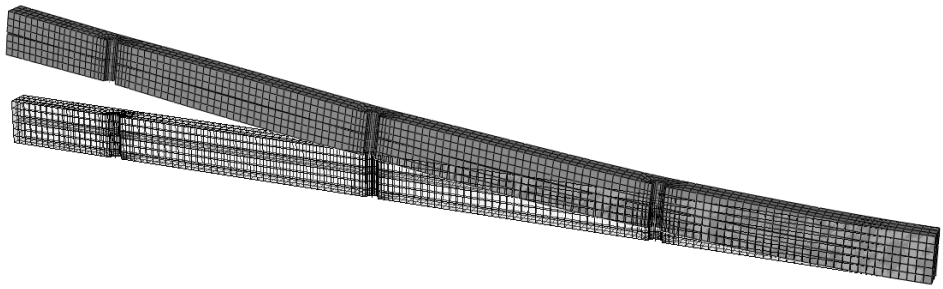

Figure 18: Finite element model of double-beam experiment. Initial configuration and static displacement (Scale factor 100)

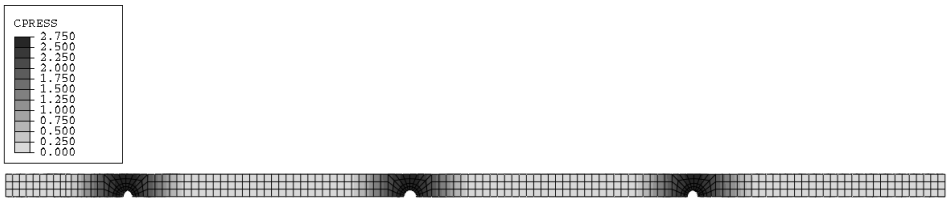

Figure 19: Normal pressure distribution

Due to the symmetry of the system with respect to the x,z-plane only half of the system is modeled, where the parts of the double-beam set-up are discretized using 1449 linear HEX8-elements each. The bolts are modeled by beam elements connected to the upper and lower beam by multi-point constraints, respectively.

The material data of the single beams have been identified from a standard modal analysis of a clamped single beam

$E = 1.67 \cdot 10^5\,\mathrm{N/mm^2}$
$\nu = 0.3$
$\rho = 7.8 \cdot 10^{-6}\,\mathrm{kg/mm^3}$

and Rayleigh damping with parameters

$\alpha = 0.3 \qquad \beta = 2 \cdot 10^{-6}$

is used to account for the material damping.

In the first load step the three bolts are prestrained in a single increment to a force of $F_B = 800\,\mathrm{N}$ each, which is equivalent to the torque controlled tensioning of the experimental set-up. The average contact pressure is then

$$\bar{p} = \frac{3F_B}{A_0} = \frac{2400\,\mathrm{N}}{4300\,\mathrm{mm^2}} = 0.55\,\mathrm{N/mm^2}\,, \tag{46}$$

with local pressures varying between $p \approx 0\,\mathrm{N/mm^2}$ between the bolts and $p \approx 2.7\,\mathrm{N/mm^2}$ in the vicinity of the bolts, see Fig. 19. This pressure distribution does not change significantly during the following steps, which justifies the assumption of a nearly invariant pressure distribution close to the local $p_{\max}$ made for the constitutive contact laws above. In the second load step the system is statically deformed in 10 equal increments by a tip load of $F_T = 15\,\mathrm{N}$ to the measured initial tip displacement of $u \approx 0.35\,\mathrm{mm}$. In the third load step this tip load is removed and the system is allowed to perform free vibrations. Time-integration is done using the undamped Newmark algorithm with standard parameters $\alpha = 0.25$ and $\beta = 0.5$. A fixed time-step of $\Delta t = 2 \cdot 10^{-4}\,\mathrm{s}$ is chosen and the system is integrated over 10^4 steps until $t = 2\,\mathrm{s}$.

4.2 Comparison of results

Comparisons between measured and simulated data for the tip displacement are shown in Figs. 20, 21, and 22, respectively. Actually the simulated data show a little higher damping than the measurement, but the agreement is very good, especially since the constitutive contact behavior has been obtained independently by the halfspace simulation.

4.3 Influence of parameters

In the following some parametric studies are presented to study the influence of the normal and tangential contact stiffness on the damping behavior. To simplify

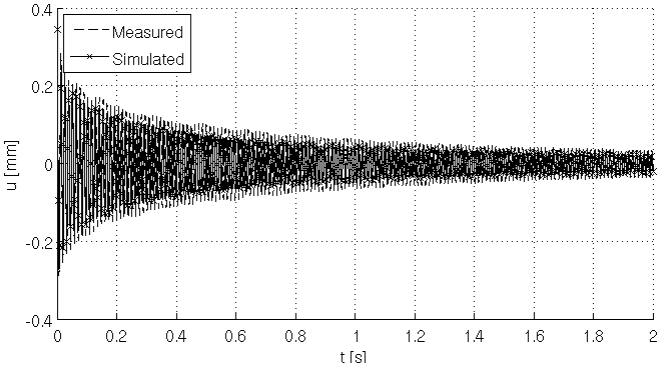

Figure 20: Decay behavior of tip displacement

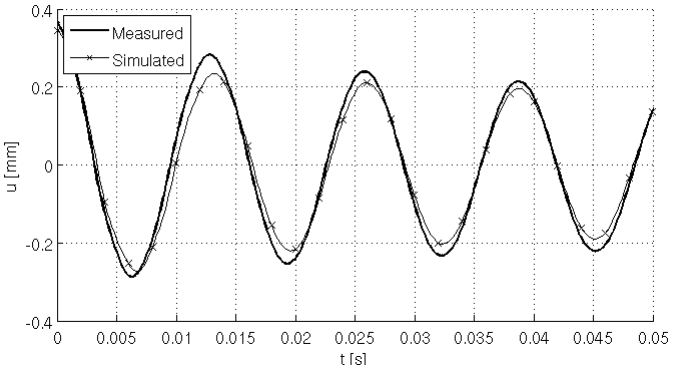

Figure 21: Zoom of short time behavior of tip displacement

the discussion, here a linear elastic pressure-gap relation with a constant normal contact stiffness is assumed instead of the nonlinear elasto-plastic relation of the original simulation.

Figure 23 shows that a varying normal stiffness at a constant slip distance does not influence the short time behavior of the dissipation, but a higher normal stiffness leads to a reduced energy dissipation in the long-time behavior, see 24. In the short time range the relative displacements are dominated by the initial configuration such that the contact interface will be mostly slipping. Here, the energy dissipation is given by the average pressure which is independent of the contact stiffness and just determined by the bolt forces. The contact stiffness does however influence the local pressure distribution, with a high stiffness leading to higher pressures localized in the vicinity of the bolts while a low stiffness leads to a more even

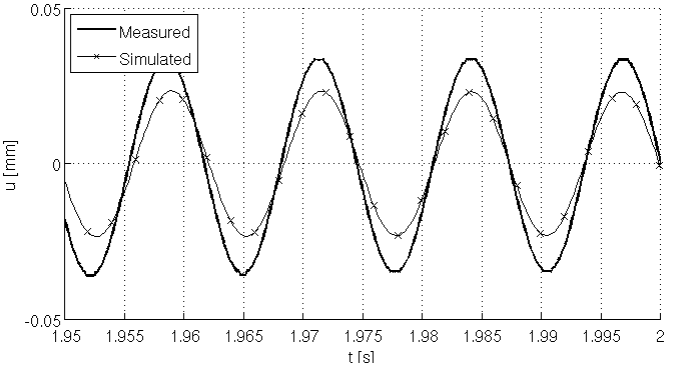

Figure 22: Zoom of long time behavior of tip displacement

distribution of the pressure, see Fig. 25 and 26. Therefore, in the long-time behavior a high stiffness will lead to a lower energy dissipation since the high-pressure areas will prevent slipping and the remaining slipping areas have only very low pressures and thus only low friction resulting in a lower dissipation.

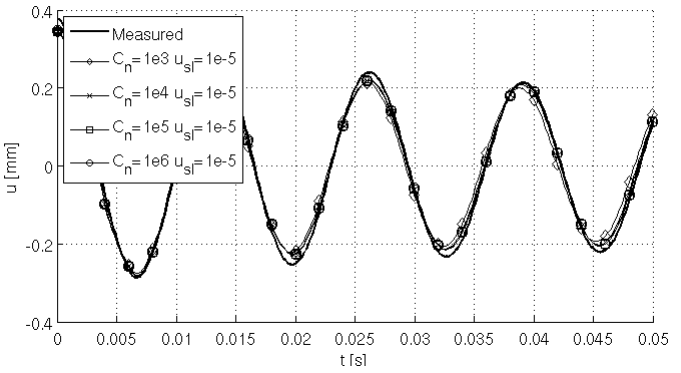

Figure 23: Influence of C_n. Zoom of short time behavior of tip displacement

Similarly, the tangential stiffness, determined by the characteristic slip distance u_{sl}, has no influence on the short time behavior, but a smaller slip distance, i.e. higher tangential stiffness, increases the damping in the long-time behavior, as can be seen in Figs. 27 and 28, respectively. At the start of the free vibration the relative displacements are relatively large, such that the contact interface will be mostly slipping. Hence, the tangential stiffness is not important. However, as the relative displacements decrease, the stick-state becomes more influential and the slip dis-

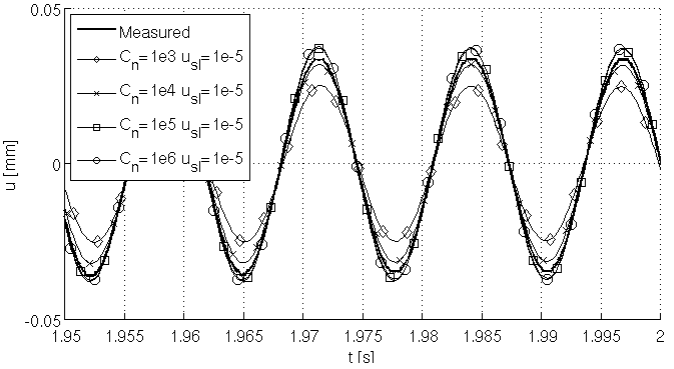

Figure 24: Influence of C_n. Zoom of long time behavior of tip displacement

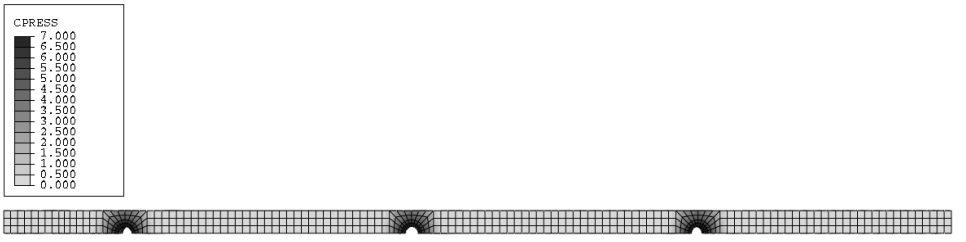

Figure 25: Normal pressure distribution for $C_n = 10^6\,\mathrm{N/mm^3}$

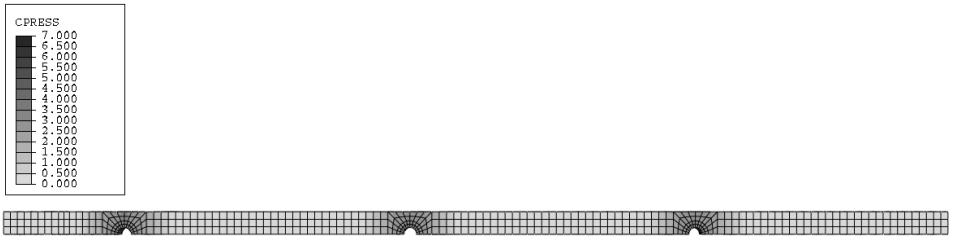

Figure 26: Normal pressure distribution for $C_n = 10^3\,\mathrm{N/mm^3}$

tance u_{sl} determines the amount of elastic relative displacement without slipping, i.e. without energy dissipation. Thus, a high value for u_{sl} means lower dissipation, while small values for u_{sl} will give higher dissipation.

Now, since both the normal as well as the tangential stiffness can be varied to change the dissipation behavior, a parameter identification or optimization using the experimental results becomes difficult. While it is possible to tune the parameters

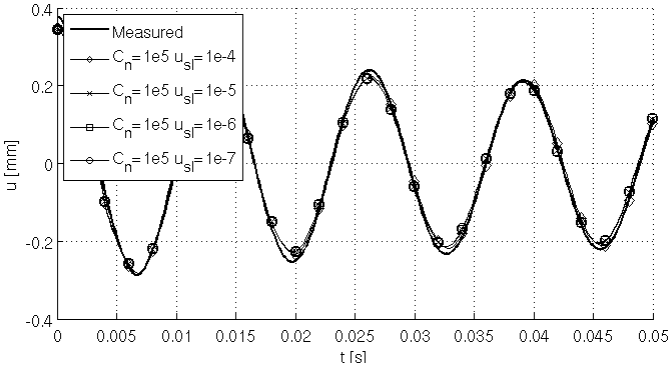

Figure 27: Influence of u_{sl}. Zoom of short time behavior of tip displacement

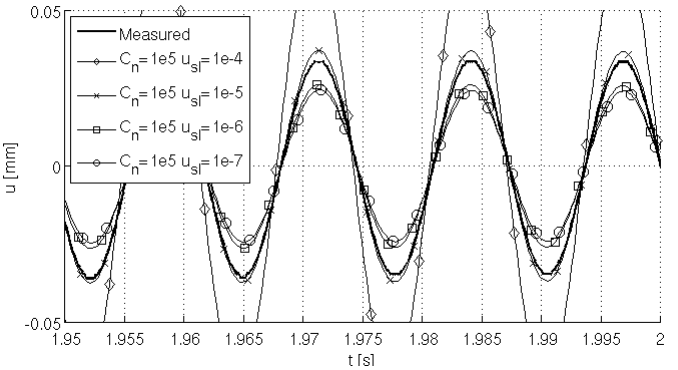

Figure 28: Influence of u_{sl}. Zoom of long time behavior of tip displacement

to obtain a nearly perfect agreement between simulated and measured result, the choice is not unique. As Fig. 29 shows using the normal law obtained from the halfspace simulations ($C_n = HS$) and a modified slip distance ($u_{sl} = 3 \cdot 10^{-5}$ mm) gives the same results as the original slip distance from the halfspace simulations ($u_{sl} = 10^{-5}$ mm) together with a modified linear stiffness ($C_n = 10^4$ N/mm^3). Other combinations are also possible.

5 Conclusions

Energy dissipation by friction in joints is the major source of damping in built-up structures. Microslip effects play an important role where only small regions of the contact surface are slipping and therefore are dissipating energy, while most of the

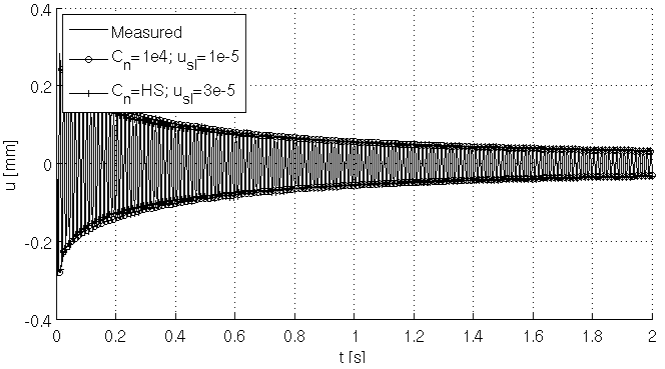

Figure 29: Non-unique parameter identification

contact area is sticking, thus ensuring the integrity of the structure.

A successful numerical simulation of a structural joint requires a sufficiently detailed description of the constitutive interface behavior. Especially an adequate description of the normal and tangential contact stiffness seems necessary, since these values dominate the amount of microslip and thus the amount of energy dissipation.

The presented elasto-plastic halfspace model allows to derive suitable constitutive contact laws which can be implemented into a standard finite-element package.

While closed form constitutive contact laws based on easy measurable parameters can be obtained for the purely elastic contact by employing the BGT-model, see Eq. 30, the assumption of a purely elastic contact is in general wrong, since most engineering surfaces will deform plastically upon initial contact. This can be described in a simple manner using the Abbott-curve or bearing area model, see Eq. 38, while the elastic unloading and reloading case taking into account the plastic predeformation can be sufficiently described by the linear relationship Eq. 39 with a pressure dependent stiffness given by Eq. 40.

However at least for the bolted structure used here, the numerical examples show that the normal contact pressure remains nearly constant during operation, such that this modeling of the unloading behavior seems not necessary.

The constitutive behavior obtained as a-priori data from a halfspace simulation of the rough surface contact gives good agreement with measured data. Especially in view of the fact that just a small part of the contact area was measured which was assumed to be representative, but no statistics over several roughness measurements have been done so far. Therefore possible scatter of the roughness data is unknown and will be taken into account only in future work.

Further effects like asperity damage, wear, and debris accumulation are not included in the present model but could be included at least in a phenomenological way into the constitutive contact laws. However, none of these effects has been observed in the beam experiments, perhaps due to the short time duration of the experiments.

An identification or verification of the contact parameters from the experiment is critical, since the identification for this single experiment is not unique. A possible way to improve this situation would be fitting the simulated data to several experimental measurements with different normal pressures to get a clearer picture of the influence of the non-linear normal stiffness. However, this is also intended future work.

References

Ahmadian, H.; Ebrahimi, M.; Mottershead, J. E.; Friswell, M. I. (2002): Identification of bolted-joint interface models. In *Proceedings of ISMA2002*, volume IV, pp. 1741–1747. K.U. Leuven.

Ahmadian, H.; Mottershead, J. E.; James, S.; Friswell, M. I.; Reece, C. A. (2006): Modelling and updating of large surface-to-surface joints in the awe-mace structure. *Mechanical Systems and Signal Processing*, vol. 20, pp. 868–880.

Allwood, J. (2005): Survey and performance assessment of solution methods for elastic rough contact problems. *Journal of Tribology*, vol. 127, pp. 10–23.

Archard, J. F. (1957): Elastic deformation and the laws of friction. *Proceedings of the Royal Society of London, Series A*, vol. 243, pp. 190–205.

Berger, E. J.; Krousgrill, C. M. (2002): On friction damping modelling using bilinear hysteresis elements. *Journal of Vibration and Acoustics*, vol. 124, pp. 367–375.

Berry, M. V.; Blackwell, T. M. (1981): Diffractal echoes. *Journal of Physics A*, vol. 14, pp. 3101–3110.

Bliman, P.-A. (1992): Mathematical study of the Dahl's friction model. *European Journal of Mechanics. A/Solids*, vol. 11, pp. 835–848.

Borri-Brunetto, M.; Carpinteri, A.; Chiaia, B. (1998): Lacunarity of the contact domain betweeen elastic bodies with rough boundaries. In Frantziskonis, G.(Ed): *PROBAMAT – 21st Century: Probabilities and Materials*, pp. 45–66, Dordrecht. Kluwer.

Bouc, R. (1957): Forced vibrations of a mechanical system with hysteresis. In *Proc. of the 4th Conference on Nonlinear Oscillations*, pg. 315.

Bush, A. W.; Gibson, R. D.; Thomas, T. R. (1975): The elastic contact of a rough surface. *Wear*, vol. 35, pp. 87–111.

Ciavarella, M.; Demelio, G.; Barber, J. R.; Jang, Y. H. (2000): Linear elastic contact of the Weierstrass profile. *Proceedings of the Royal Society of London, Series A*, vol. 456, pp. 387–405.

Dahl, P. (1976): Solid friction damping of mechanical vibrations. *AIAA Journal of Guidance, Control, and Dynamics*, vol. 14, pp. 1675–1682.

de Wit, C. C.; Olsson, H.; Aström, K. J.; Lischinsky, P. (1995): A new model for control of systems with friction. *IEEE Transactions on Automatic Control*, vol. 40, pp. 419–425.

Dohner, J. L. (2001): On the development of methodologies for constructing predictive models of structures with joints and interfaces. White Paper SAND2001-0003P, Sandia National laboratories, Albuquerque, 2001.

Dydo, J. R.; Busby, H. R. (1995): Elasticity solutions for constant and linearly varying loads applied to a rectangular surface patch on the elastic halfspace. *Journal of Elasticity*, vol. 38, pp. 153–163.

Earles, S. W.; Beards, C. F. (1970): Some aspects of frictional damping as applied to vibrating beams. *International Journal of Machine Tool Design and research*, vol. 10, pp. 123–131.

Feeny, B.; Guran, A.; Hinrichs, N.; Popp, K. (1998): A historical review on dry friction and stick-slip phenomena. *Applied Mechanics Reviews*, vol. 51, pp. 321–341.

Ferri, A. A.; Bindemann, A. C. (1992): Damping and vibration of beams with various types of frictional support conditions. *Journal of Vibration and Acoustics*, vol. 114, pp. 289–296.

Garikipati, K. (2002): A variational multiscale method to embed micromechanical surface laws in the macromechanical continuum formulation. *CMES: Computer Modeling in Engineering & Sciences*, vol. 3, pp. 175–184.

Gaul, L.; Lenz, J. (1997): Nonlinear dynamics of structures assembled by bolted joints. *Acta Mechanica*, vol. 125, no. 169-181.

Gaul, L.; Nitsche, R. (2000): Dynamics of structures with joint connections. In Ewins, D. J.; Inman, D. J.(Eds): *Structural Dynamics @ 2000: Current Status and Future Directions*, pp. 29–48.

Gaul, L.; Nitsche, R. (2001): Role of friction in mechanical joints. *Applied Mechanics Reviews*, vol. 54, pp. 93–105.

Görke, D.; Willner, K. (2008): Experimental setup for normal contact stiffness measurement of technical surfaces with geometrical irregularities. *Experimental Techniques*.

Görke, D.; Willner, K. (2008): Normal contact of fractal surfaces – Experimental and numerical investigations. *Wear*, vol. 264, pp. 589–598.

Hanss, M.; Oexl, S.; Gaul, L. (2002): Identification of a bolted-joint model with fuzzy parameters loaded normal to the contact interface. *Mechanics Research Communications*, vol. 29, no. 2/3, pp. 177–187.

Ibrahim, R. A.; Pettit, C. L. (2005): Uncertainties and dynamic problems of bolted joints and other fasteners. *Journal of Sound and Vibration*, vol. 279, pp. 857–936.

Ikhouane, F.; Rodellar, J. (2007): *Systems with Hysteresis*. Wiley, Chichester.

Iwan, W. D. (1966): On distributed-element model for hysteresis and its steady-state dynamic response. *Journal of Applied Mechanics*, vol. 33, pp. 893–900.

Iwan, W. D. (1967): On a class of models for the yielding behaviour of continuous and composite systems. *Journal of Applied Mechanics*, vol. 34, no. 3, pp. 612–617.

Jackson, R. L.; Kogut, L. (2006): A comparison of flattening and indentation approaches for contact mechanics modeling of single asperity contacts. *Journal of Tribology*, vol. 128, pp. 209–212.

Jacq, C.; Nelias, D.; Lormand, G.; Girodin, D. (2002): Development of a three-dimensional semi-analytical elastic-plastic contact code. *Journal of Tribology*, vol. 124, pp. 653–667.

Jalali, H.; Ahmadian, H.; Mottershead, J. E. (2007): Identification of nonlinear bolted lap-joint paramters by force-state mapping. *International Journal of Solids and Structures*, vol. 44, pp. 8087–8105.

Jenkin, C. F. (1922): A mechanical model illustrating the behaviour of metals under static and alternating loads. *Engineering*, vol. 17, pp. 603.

Ju, Y.; Farris, T. N. (1996): Spectral analysis of two-dimensional contact problems. *Journal of Tribology*, vol. 118, pp. 320–328.

Kalker, J. J. (1977): Variational principles of contact elastostatics. *Journal of the Institute of Mathematics and its Applications*, vol. 20, pp. 199–219.

Kalker, J. J. (1979): The computation of three-dimensional rolling contact with dry friction. *International Journal for Numerical Methods in Engineering*, vol. 14, pp. 1293–1307.

Kalker, J. J. (1990): *Three-Dimensional Elastic Bodies in Rolling Contact*. Springer, Heidelberg.

Kalker, J. J.; van Randen, Y. (1972): A minimum principle for frictionless elastic contact with application to non-Hertzian half-space contact problems. *Journal of Engineering Mathematics*, vol. 6, pp. 193–206.

Karpenko, Y. A.; Akay, A. (2002): A numerical method for analysis of extended rough wavy surfaces in contact. *Journal of Tribology*, vol. 124, pp. 668–679.

Komvopoulos, K.; Ye, N. (2001): Three-dimensional contact analysis of elastic-plastic layered media with fractal surface topographies. *Journal of Tribology*, vol. 123, pp. 632–640.

Lee, S. C.; Ren, N. (1996): Behavior of elastic-plastic rough surface contacts as affected by surface topography, load and material hardness. *Tribology Transactions*, vol. 39, pp. 67–74.

Lenz, J.; Gaul, L. (1995): The influence of microslip on the dynamic behaviour of bolted joints. In *Proceedings of the 13th IMAC, Nashville, Tennessee*, volume I, pp. 248–254.

Li, J.; Berger, E. (2001): A Boussinesq-Cerutti solution set for constant and linear distribution of normal and tangential load over triangular area. *Journal of Elasticity*, vol. 63, pp. 137–151.

Li, J.; Berger, E. (2003): A semi-analytical approach to three-dimensional normal contact problems with friction. *Computational Mechanics*, vol. 30, pp. 310–322.

Ling, F. F. (1987): Scaling law for contoured length of engineering surfaces. *Journal of Applied Physics*, vol. 62, pp. 2570–2572.

Lobitz, D. W.; Gregory, D. L.; Smallwood, D. O. (2001): Comparison of finite element predictions to measurements from the sandia microslip experiment. In

Proc. of the International Modal Analysis Conference IMAC XX, Los Angeles, pp. 1388–1394.

Ma, X.; Bergman, L.; Vakakis, A. (2001): Identification of bolted joints through laser vibrometry. *Journal of Sound and Vibration*, vol. 246, pp. 441–460.

Mackerle, J. (2003): Finite element analysis of fastening and joining: A bibliography (1990-2002). *International Journal of Pressure Vessels and Piping*, vol. 80, pp. 253–271.

Majumdar, A.; Tien, C. L. (1990): Fractal characterization and simulation of rough surfaces. *Wear*, vol. 136, pp. 313–327.

Mandelbrot, B. (1983): *The Fractal Geometry of Nature*. Freeman, New York.

Mayer, M. H.; Gaul, L. (2007): Segment-to-segment contact elements for modelling joint interfaces in finite element analysis. *Mechanical Systems and Signal Processing*, vol. 21, pp. 724–734.

Menq, C. H.; Bielak, J.; Griffin, J. H. (1986): The influence of microslip on vibratory response. *Journal of Sound and Vibration*, vol. 107, no. 2, pp. 279–307.

Miller, J. D.; Quinn, D. D. (2009): A two-sided interface model for dissipation in structural systems with frictional joints. *Journal of Sound and Vibration*, vol. 321, pp. 201–219.

Mindlin, R. D. (1949): Compliance of elastic bodies in contact. *Journal of Applied Mechanics*, vol. 16, pp. 259–268.

Nelias, D.; Antaluca, E.; Boucly, V.; Cretu, S. (2007): A three-dimensional semianalytical model for elastic-plastic sliding contacts. *Journal of Tribology*, vol. 129, pp. 761–771.

Ogilvy, J. A. (1992): Numerical simulation of elastic-plastic contact between anisotropic rough surfaces. *Journal of Physics D*, vol. 25, pp. 1798–1809.

Pian, H.; Hallowell, C. (1951): Structural damping in a simple built-up beam. In *Proceedings of the first US Congress of Applied Mechanics*.

Polonsky, I. A.; Keer, L. M. (2000): A fast and accurate method for numerical analysis of elastic layered contacts. *Journal of Tribology*, vol. 122, pp. 30–35.

Polonsky, I. A.; Keer, L. M. (2000): Fast methods for solving rough contact problems: A comparative study. *Journal of Tribology*, vol. 122, pp. 36–41.

Quinn, D. D.; Segalman, D. J. (2005): Using series-series Iwan-type models for understanding joint dynamics. *Journal of Applied Mechanics*, vol. 72, pp. 666–673.

Ren, N.; Lee, S. C. (1993): Contact simulation of three-dimensional rough surfaces using moving grid method. *Journal of Tribology*, vol. 115, pp. 597–601.

Ren, N.; Lee, S. C. (1994): The effects of surface roughness and topography on the contact behavior of elastic bodies. *Journal of Tribology*, vol. 116, pp. 804–811.

Sainsot, P.; Jacq, C.; Nelias, D. (2002): A numerical model for elastoplastic rough contact. *CMES: Computer Modeling in Engineering & Sciences*, vol. 3, pp. 497–506.

Sayles, R. S. (1996): Basic principles of rough surface contact analysis using numerical methods. *Tribology International*, vol. 29, pp. 639–650.

Segalman, D. J. (2005): A four-parameter Iwan model for lap-type joints. *Journal of Applied Mechanics*, vol. 72, pp. 752–760.

Segalman, D. J. (2006): Modelling joint friction in structural dynamics. *Structural Control and Health Monitoring*, vol. 13, pp. 430–453.

Segalman, D. J.; Paez, T.; Smallwood, D.; Sumali, A.; Urbina, A. (2003): Status and integrated road-map for joints modeling research. Sandia report sand2003-0897, Sandia National Laboratories, 2003.

Sellgren, U.; Olofsson, U. (1999): Application of a constitutive model for micro-slip in finite element analysis. *Computer Methods in Applied Mechanics and Engineering*, vol. 170, pp. 65–77.

Song, Y.; Hartwigsen, C. J.; McFarland, D. M.; Vakakis, A. F.; Bergman, L. A. (2004): Simulation of dynamics of beam structures with bolted joints using adjusted Iwan beam elements. *Journal of Sound and Vibration*, vol. 273, pp. 249–276.

Song, Y.; McFarland, D. M.; Bergman, L. A.; Vakakis, A. F. (2005): Stick-slip-slap interface response simulation: Formulation and application of a general joint/interface element. *CMES: Computer Modeling in Engineering & Sciences*, vol. 10, pp. 153–170.

Stanley, H. M.; Kato, T. (1997): An FFT-based method for rough surface contact. *Journal of Tribology*, vol. 119, pp. 481–485.

Tian, X.; Bhushan, B. (1996): A numerical three-dimensional model for the contact of rough surfaces by variational principle. *Journal of Tribology*, vol. 118, pp. 33–42.

Varadi, K.; Neder, Z. (1996): Three-dimensional contact analysis of real rough surfaces. In Bartz, W. J.(Ed): *Tribology - Solving Friction and Wear Problems*, volume 2, pp. 1037–1046, Ostfildern. Technische Akademie Esslingen.

Vollebregt, E. A. H. (1995): A Gauss-Seidel type solver for special convex programs, with application to frictional contact mechanics. *Journal of Optimization Theory and Applications*, vol. 87, pp. 47–67.

Wang, F.; Keer, L. M. (2005): Numerical simulation for three dimensional elastic-plastic contact with hardening behavior. *Journal of Tribology*, vol. 127, pp. 494–502.

Wang, S.; Komvopoulos, K. (1994): A fractal theory of the interfacial temperature distribution in the slow sliding regime: Part I – elastic contact and heat transfer analysis. *Journal of Tribology*, vol. 116, pp. 812–823.

Warren, T. L.; Krajcinovic, D. (1996): Random Cantor set models for the elastic-perfectly plastic contact of rough surfaces. *Wear*, vol. 196, pp. 1–15.

Webster, M. N.; Sayles, R. S. (1986): A numerical model for the elastic frictionless contact of real rough surfaces. *Journal of Tribology*, vol. 108, pp. 314–320.

Wen, Y. K. (1989): Methods of random vibrations for inelastic structures. *Applied Mechanics Reviews*, vol. 42, pp. 39–52.

Willner, K. (2004): Elasto-plastic normal contact of three-dimensional fractal surfaces using halfspace theory. *Journal of Tribology*, vol. 126, pp. 28–33.

Willner, K. (2008): Fully coupled frictional contact using elastic halfspace theory. *Journal of Tribology*, vol. 130, pp. 031405–1–031405–8.

Willner, K. (2008): Influence of surface parameters on the elastoplastic contact behavior of fractal-regular surfaces. *Journal of Tribology*, vol. 130, pp. 024502–1–024502–6.